Available online at www.sciencedirect.com
ScienceDirect
Trans. Nonferrous Met. Soc. China 35(2025) 2553−2571
Transactions of Nonferrous Metals Society of China
www.tnmsc.cn

Superplasticity of fine-grained Mg−Gd−Y−Zn−Zr alloy prepared via multi-directional forging

Jing-qi ZHAO[1], Ze-zheng WANG[1], Chun KE[1], Qiang MENG[1], Chun-xiang ZHANG[2], Jun-ting LUO[1,2]

1. Key Laboratory of Advanced Forging & Stamping Technology and Science, Ministry of Education, School of Mechanical Engineering, Yanshan University, Qinhuangdao 066004, China;
2. State Key Laboratory of Metastable Materials Science and Technology, Yanshan University, Qinhuangdao 066004, China

Received 1 January 2024; accepted 30 August 2024

Abstract: The superplasticity of the Mg−8.59Gd−3.85Y−1.14Zn−0.49Zr alloy was investigated before and after multi-directional forging (MDF) and the mechanisms affecting superplastic deformation were analyzed. The results indicate that after MDF at a temperature of 350 °C and strain rates of 0.1 and 0.01 s^{-1} (1-MDFed and 2-MDFed), the superplasticity of the alloy can be significantly improved. The elongations of the MDFed alloys exceed 400% under the strain rate of 6.06×10^{-4} s^{-1} and temperatures of 350, 375, and 400 °C, and reach the maximum values of 766% (1-MDFed) and 693% (2-MDFed) at 375 °C. The grain boundary sliding of the MDFed alloy is sufficient, and the energy barrier of deformation decreases. The β phase limits the grain growth and promotes dynamic recrystallization, maintaining the stability of the fine-grained structure during superplastic deformation. Several Y-rich phases nucleate in the high-strain region (i.e., the final fracture region) at high temperatures, accelerating the fracture of the specimen.
Key words: Mg−Gd−Y−Zn−Zr; superplasticity; multi-directional forging; fracture morphology; Y-rich phase

1 Introduction

Magnesium alloys exhibit lower densities, higher specific strength and specific stiffness than common steel and aluminium alloys, and have broad application prospects [1,2]. However, magnesium alloys have a hexagonal close-packed structure and, therefore, exhibit low plasticity at room temperature [3,4]. These alloys are difficult to process via the traditional plastic-forming process, and the currently popular die-casting process cannot yield high-quality products. These issues are obstacles to the large-scale industrialization of magnesium alloys. For products with complex structures made of such difficult-to-deform materials, superplastic forming has gradually become a recognized and effective method for achieving both high production efficiency and performance [5].

Superplasticity is a phenomenon by which materials exhibit abnormally low rheological resistance and excellent rheological properties in the presence of certain internal structures and external conditions [6]. The criterion for achieving superplasticity is that elongation must exceed 200% [7]. The mechanism associated with superplastic deformation can be determined using the strain rate sensitivity index (m) [8,9]. When m is in the range of 0.3−0.7, grain boundary sliding (GBS), an important mechanism associated with superplastic deformation, is activated [5,10]. Another important parameter to be considered is the deformation activation energy (Q), an essential reference for

Corresponding author: Jun-ting LUO, Tel/Fax: +86-335-8052253, E-mail: luojunting@ysu.edu.cn
https://doi.org/10.1016/S1003-6326(25)66832-4

determining the auxiliary mechanism associated with superplasticity [11]. To achieve high elongation, the vacancies generated during the GBS process must be regulated by the auxiliary mechanism. At present, research on the superplasticity of magnesium alloys focuses on fine-grained superplasticity [5,12]. The grain boundary density of a unit volume of a fine-grained structure is high, which can effectively coordinate GBS and disperse stress [5,13]. To achieve a fine-grained structure, deformation and heat treatment processes must be improved and integrated [14,15] in addition to optimizing the composition and proportion of the constituent elements [16,17]. In this context, multi-directional forging (MDF) has been widely explored owing to its simple principle, low cost, and ability to impart an excellent microstructure-refinement effect. CAO et al [18] refined the grain size of the Mg−10.2Li−2.1Al−2.23Zn−0.2Sr alloy from 125 to 3.75 μm using a combination of MDF, rolling, and annealing and achieved an excellent elongation of approximately 712.1% at 350 °C. MEHRABI et al [19] employed extrusion and MDF to refine the grain size of the Mg−8Li−1Zn alloy from 8 to 4 μm and verified superplasticity via shear impact tests.

Superplastic deformation is a process that requires a long duration and high temperatures, and the stability of the fine-grained structure is essential for the sustainability of deformation [7]. LEE and KIM [20] obtained ultrafine-grained Mg−Y−Zn−Zr alloys with grain sizes of 1.1 and 1 μm via high-ratio differential speed rolling (HRDSR) with roll speed ratios of 2 and 3, respectively; HRDSR3 with many *I* phases exhibited large elongations below 250 °C as the “pinning” of the *I* phase maintained the stability of the structure. However, the *I* phase dissolved at high temperatures, the structure coarsened, and the elongation decreased. The stability of the fine-grained structure can be maintained with the intergranular second phase. However, the associated mechanism is easily affected by the stability of this phase. In addition, the volume fraction and structural characteristics of the second phase significantly impact the superplastic deformation of the material. YANG et al [21] explored the superplasticity of the fine-grained Mg−10Gd−3Y−0.5Zr alloy prepared via friction stirring and identified that although the high volume fraction of β phases could effectively inhibit coarsening, stress concentration and cavity nucleation were easy to initiate. For the long-period stacking ordered (LPSO) phase, unique to the Mg−RE−Zn alloy, the elastic modulus and hardness are higher than those of the magnesium matrix. A related study [22] identified cavities nucleated at the boundaries of large-sized LPSO phases.

In a previous study [23], a type of fine-grained Mg−Gd−Y−Zn−Zr alloy was treated with MDF, and the grain structure was further refined. The Mg−Gd−Y−Zn−Zr alloy is one of the magnesium alloys with the best mechanical properties, combining the strengthening mechanisms of various rare-earth elements [24]. Several studies [25−27] have reported the complex microstructural evolution behavior of such a rare-earth magnesium alloy during hot deformation; however, only a few studies [9,28] related to superplasticity, particularly that of the alloy prepared via severe plastic deformation, exist. Therefore, relevant studies must be conducted to address this research gap. Furthermore, as aforementioned, the second phase has a significant impact on the superplastic deformation of an alloy, and the Mg−Gd−Y−Zn−Zr alloy has multiple types of second phases owing to the addition of rare-earth elements. Therefore, the role of these second phases must be determined.

This work explored the superplasticity of the Mg−Gd−Y−Zn−Zr alloy before and after MDF via the high-temperature tensile test and analyzed the effects of the microstructural evolution and precipitation mechanisms of the second phases on superplastic deformation. The obtained findings can serve as a valuable reference for investigating the superplastic behavior of this rare-earth magnesium alloy.

2 Experimental

MDF billets were obtained from an extruded bar of a fine-grained rare-earth magnesium alloy with a nominal composition of Mg−8.59Gd−3.85Y−1.14Zn−0.49Zr (wt.%). MDF was performed at 350 °C under strain rates of 0.1 and 0.01 s^{-1} [23], and the products were defined as 1-MDFed and 2-MDFed alloys, respectively. The number of MDF passes was 9, with a reduction of 25% per pass and a cumulative strain of approximately 2.6, which further refined the average grain size of the alloy from 4.10 μm before MDF to 2.95 and 3.27 μm

after MDF [23]. The tensile specimen of the alloy before MDF (defined as the original alloy) was cut from the longitudinal section of the extruded bar, and the long axis of the original specimen was parallel to the axial direction of the bar. The tensile specimens of the 1-MDFed and 2-MDFed alloys were cut along the plane perpendicular to the forging direction of the last pass in the center of the MDFed billets. The tensile specimen has a dog-bone shape, as shown in Fig. 1. The high-temperature tensile test was conducted using an Inspekt 100 electronic universal high-temperature testing machine. The test temperatures were set as 300, 350, 375 and 400 °C, and the tensile velocity was 0.2 mm/min, i.e., the strain rate was 6.06×10^{-4} s^{-1}. The strain distribution characteristics of the specimens during the high-temperature tensile process were obtained using a digital image correlation (DIC) measuring instrument. The metallographic images of the specimens before and after being subjected to the tensile test were obtained using a ZEISS-AX10 metallographic optical microscope (OM). An S−3400N scanning electron microscope (SEM) was used to observe the gauge section and fracture surface of the tensile specimens, and the microstructures of these specimens were characterized using a JOEL−2010 transmission electron microscope (TEM).

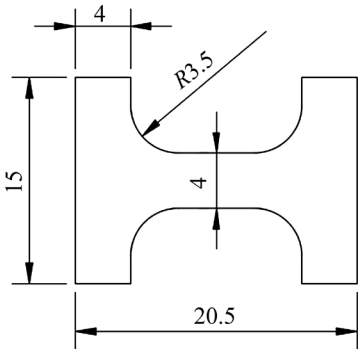

Fig. 1 Sizes of tensile specimen (unit: mm)

3 Results and discussion

3.1 High-temperature tensile curves of alloys before and after MDF

The high-temperature tensile engineering stress−strain curves of the original alloy are presented in Fig. 2. Flow stress decreases with the increase of test temperature, and the flow stresses at 375 and 400 °C exhibit a steady-state stage. The elongations of the specimens at 350, 375 and 400 °C are 193%, 269% and 338%, respectively, i.e., the alloy exhibits superplasticity before MDF.

The high-temperature tensile curves of the MDFed alloys are presented in Fig. 3. The tensile test temperature of the MDFed alloy included an

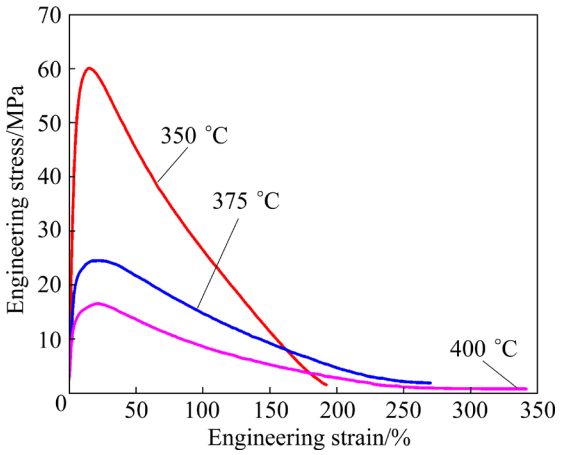

Fig. 2 High-temperature tensile engineering stress−strain curves of original alloy

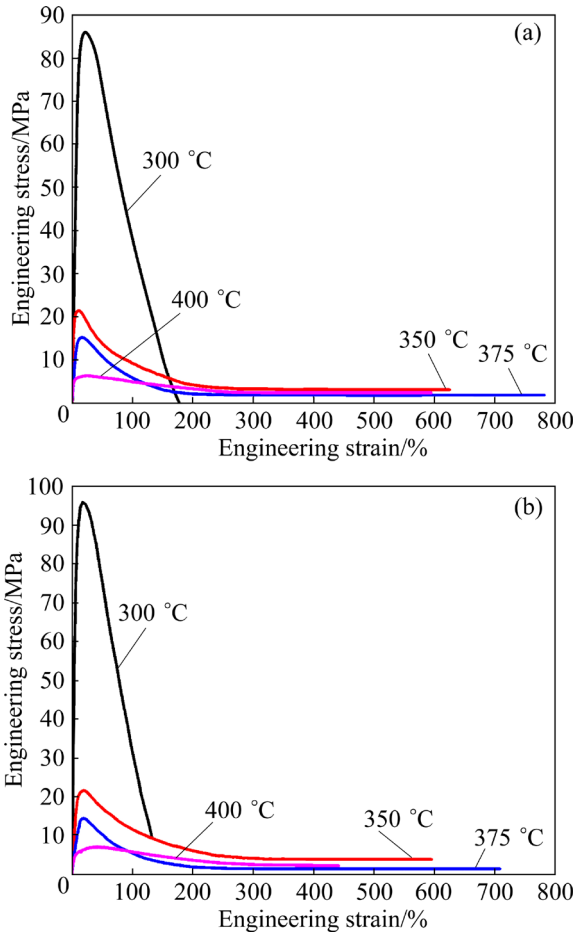

Fig. 3 High-temperature tensile engineering stress–strain curves of MDFed alloys: (a) 1-MDFed; (b) 2-MDFed

additional 300 °C. At 300 °C, the flow stress is high and elongation is low concerning those obtained from the other curves in the figure. At the same temperature, the flow stress of the MDFed alloy is significantly lower than that of the original alloy, and the flow stress exhibits a steady-state stage. In addition, the elongation considerably increases. The elongations of all groups of specimens exceed 400%, except for the specimens tested at 300 °C, which exhibits elongations lower than 200%. The elongations increase with the increase in test temperature and reach the maximum at 375 °C. The elongations of the 1-MDFed and 2-MDFed specimens reach 766% and 693%, respectively. As the temperature increases to 400 °C, the elongation decreases. The images of the tensile specimens in the initial state and the fractured high-temperature tensile specimens are presented in Fig. 4. The gauge sections of the fractured specimens that achieve superplasticity are in a uniform–diffusion–elongation state without obvious local necking. In summary, MDF substantially improves the superplastic deformation ability of this type of fine-grained Mg−Gd−Y−Zn−Zr alloy.

3.2 Strain rate sensitivity index (*m*) and deformation activation energy (*Q*)

Notably, *m*, as expressed in Eq. (1), is an important parameter for measuring the superplasticity of materials [9,29]. When the *m* value of a material is high, flow stress during the deformation process will significantly increase with the increase in strain, thereby hindering the expansion of necking, and the material can achieve a stable uniform-extension deformation.

$$m=\frac{\mathrm{d}\lg\sigma}{\mathrm{d}\lg\dot{\varepsilon}} \tag{1}$$

where σ is the flow stress, and $\dot{\varepsilon}$ is the strain rate.

The velocity mutation method was employed to determine the *m* value [30], and the schematic diagram of the velocity–mutation load–strain curve is shown in Fig. 5. First, the specimen is stretched at a constant velocity v_1. When 20%−50% strain is achieved, v_1 is immediately increased to v_2, and the velocity mutation increases the load to that of Point *A* (P_A). Assuming that the specimen is stretched to the same strain as that of P_A at a constant velocity v_1, the load is extended to that of Point *B* (P_B). The *m* value can be obtained using Eq. (2). The temperatures

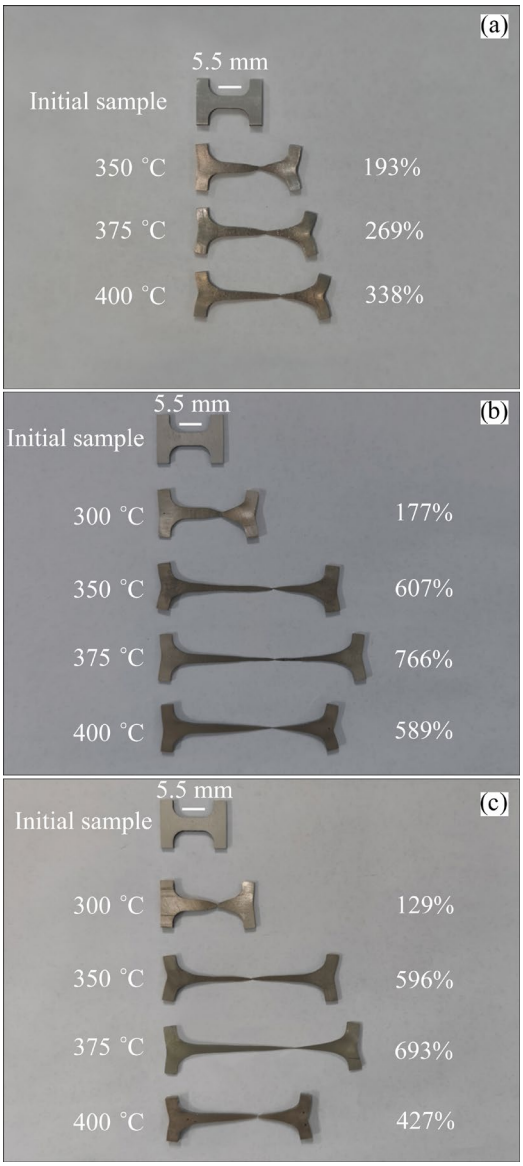

Fig. 4 Images of tensile specimens in initial state and fractured high-temperature tensile specimens: (a) Original alloy; (b) 1-MDFed; (c) 2-MDFed

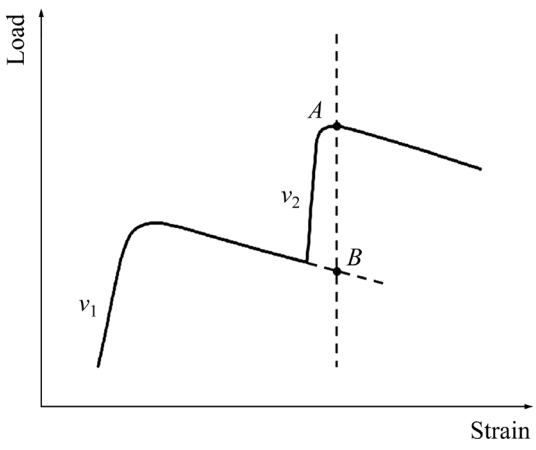

Fig. 5 Schematic diagram of load–strain curve

set during the velocity mutation test were 350, 375 and 400 °C, which are consistent with those used for the high-temperature tensile test, and the temperature set during the velocity mutation test on the MDFed alloys included an additional 300 °C. The velocity mutation was set once, and the two-stage tensile velocities were v_1=0.2 mm/min and v_2=2 mm/min, i.e., the strain rates were 6.06×10^{-4} s^{-1} and 6.06×10^{-3} s^{-1}, respectively.

$$m=\ln(P_A/P_B)/\ln(v_2/v_1) \quad (2)$$

Figure 6(a) depicts the calculated m values. During the mutation from v_1 to v_2, the m values of the alloys at each test temperature are consistent with the constant-velocity tensile elongation at this temperature. When the elongation is less than 200% (the original alloy: 350 °C, and MDFed alloys: 300 °C), the m values are below 0.3 and GBS is inactive. At the other temperatures, the alloys in different states exhibit superplasticity and the m values are higher than 0.3. The m values of the alloys before and after MDF are in the ranges of 0.4−0.5 and 0.5−0.7, respectively, suggesting that GBS is fully activated and high elongation can be achieved. The reciprocal of the m value is defined as the stress exponent (n), which is presented in Fig. 6(b). At the temperatures at which the alloy achieves superplasticity, the n values of the MDFed alloys are in the range of 1.5−2.0, suggesting that the corresponding superplastic deformation mechanism is GBS accompanied by vacancy diffusion creep [31]. Contrarily, the n values of the original alloy are in the range of 2.0−2.5, suggesting that the GBS process is affected by dislocation creep, which is consistent with low superplastic elongation.

Q values are calculated based on Eq. (3) [11]. The fitting curves depicting $\ln\sigma$ vs T^{-1} of the alloys before and after MDF at each tensile test temperature are presented in Fig. 7(a). Here, T denotes the temperature. The slope of the fitting curve is $\partial(\ln\sigma)/\partial(T^{-1})$, which can be substituted into Eq. (3) to obtain the corresponding Q value, as presented in Fig. 7(b). The Q values of the alloys in different states at each temperature are inversely proportional to the corresponding elongations. A large elongation corresponds to a low Q value, i.e., the energy barrier of deformation is low. The Q

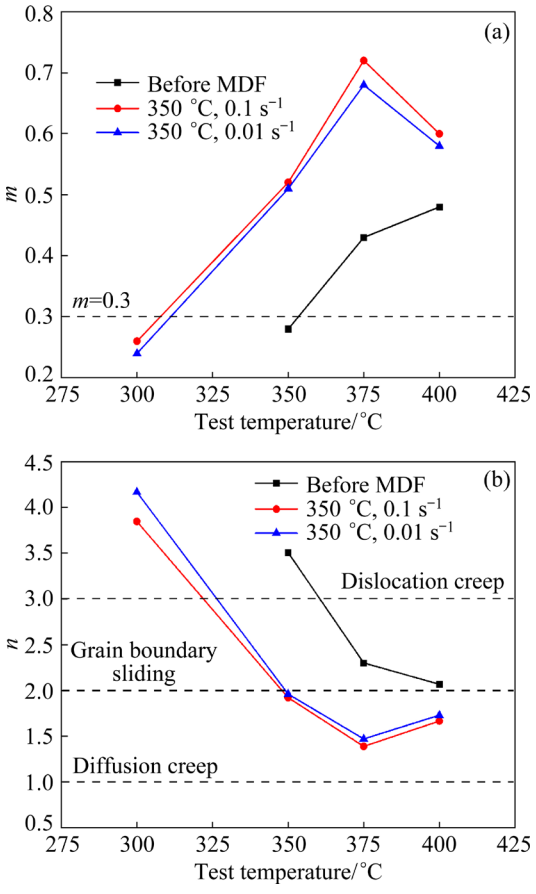

Fig. 6 Calculated m (a) and n (b) values

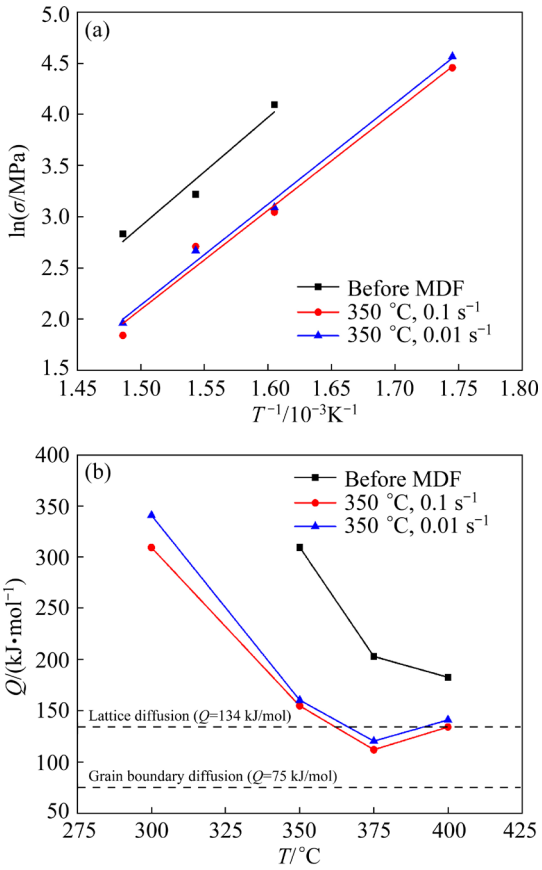

Fig. 7 Fitting curves depicting $\ln\sigma$ vs T^{-1} (a) and calculated Q values (b)

values of the MDFed alloys are between 50 and 150 kJ/mol lower than those before MDF at the same temperatures. The Q values of the two groups of MDFed alloys at 375 °C corresponding to the best elongations are 111.8 and 120.3 kJ/mol, suggesting that the diffusion creep process of the alloy mainly involves grain boundary diffusion (75.0 kJ/mol < Q < 134.0 kJ/mol) [11]. The Q values of 1-MDFed and 2-MDFed alloys at 350 °C are respectively 154.7 and 160.4 kJ/mol, suggesting that the diffusion creep process is mainly dominated by lattice diffusion (Q > 134.0 kJ/mol) [11]. The Q values of 1-MDFed and 2-MDFed alloys at 400 °C are respectively 134.1 and 141.1 kJ/mol, suggesting that both diffusion mechanisms play important regulatory roles at this temperature.

$$Q = nR\frac{\partial(\ln\sigma)}{\partial(1000/T)} \tag{3}$$

3.3 Microstructural evolution

The OM metallographic images showing the gauge section of the original specimen before tensile are presented in Fig. 8. The long axis of the specimen is parallel to the axis of the extrusion rod, and the lamellar LPSO, bulk LPSO, and α-Mg matrix are distributed along the long axis of the specimen. The proportion of the matrix structure is low, and the grains are equiaxed with an average size of approximately 4.10 μm. Small, spherical β phases demonstrate dispersive distribution at the grain boundaries and within some grains. Thresholding the metallographic images reveals that the estimated proportion of β phases in the matrix structure is 15.14%. The types of phases in this alloy was determined in a previous study [23].

Figure 9 presents the OM metallographic images depicting the gauge sections of the MDFed specimens before the tensile test. Unlike in the case of the original alloy, the LPSO phases in the MDFed alloys are substantially refined and randomly dispersed. The matrix structure is noticeably refined (1-MDFed: 2.95 μm; 2-MDFed: 3.27 μm), and the matrix proportion and the proportion of β phases (1-MDFed: 20.13%; 2-MDFed: 19.58%) increase.

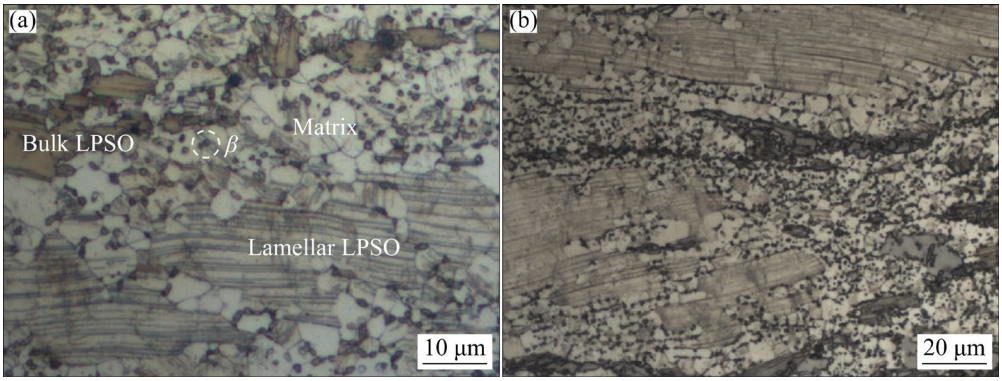

Fig. 8 OM metallographic images depicting gauge section of original specimen before tensile test: (a) High magnification; (b) Low magnification

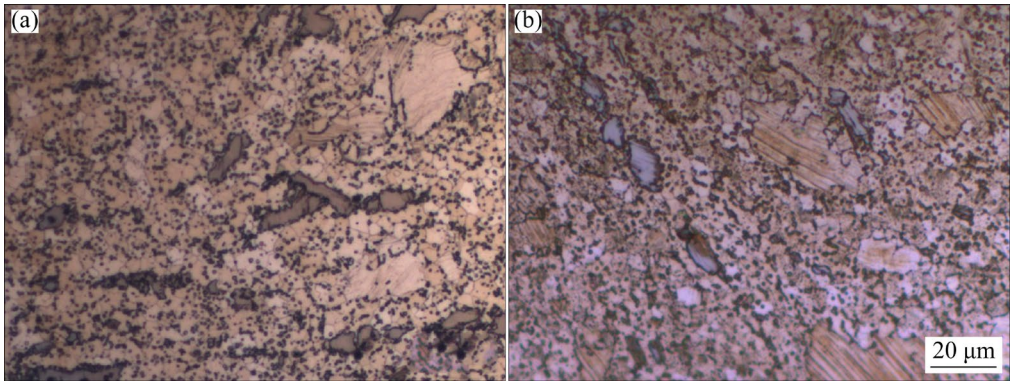

Fig. 9 OM metallographic images depicting gauge sections of MDFed specimens before tensile test: (a) 1-MDFed; (b) 2-MDFed

Figure 10 presents the OM metallographic images depicting the gauge section of the original specimen after the tensile test at 400 °C. High-temperature deformation promotes dynamic recrystallization (DRX), and small DRX grains exist around LPSO phases and irregular large-sized grains. DRX can promote the refinement of the two types of LPSO phases and increase the proportion of the matrix structure [23,32]. Figures 10(a) and (b) present the difference in the microstructural evolution near and far from the fracture surface region. The proportion of the matrix structure near the fracture surface increases more than that far from this surface. During the tensile process, the gauge section of the specimen is the main deformation zone, and the cross-section of specimen decreases with the increase in elongation. Figure 11 presents the strain distribution of the gauge section obtained using the DIC measuring instrument. The maximum strain is observed at the narrowest region of the gauge section, i.e., the final fracture zone, and the strain decays along the long axis toward either side of this region. Under a large strain, the DRX and mechanical crushing degrees near the fracture surface are high, thereby generating the aforementioned differences in the microstructure. In addition, the grain size of the matrix near the fracture surface is lower than that far from this surface (4.29 and 5.64 μm, respectively). The high temperature over a long duration during the tensile process promotes the migration of grain boundaries, which results in the growth of original and new DRX grains. This evolution exerts a substantial effect and occurs in various regions of the specimen. The actual grain size is influenced by both the growth and refinement mechanisms. The dispersed β phases in the alloy can directly hinder the migration of grain boundaries. After the high-temperature tensile test, the proportions of β phases near and far from the fracture surface are approximately 18.82% and 13.38%, respectively. Based on several discrete elements, i.e., the original ones in the microstructure and those generated by the refinement of LPSO, the dynamic precipitation of β phases is observed during hot deformation; however, the solid solubility of Gd and Y in the magnesium matrix increases with the increase in temperature, resulting in the decrease in nucleation rate and softening or even dissolution of the original β phases [21]. The large strain near the fracture surface is beneficial for the enhancement of dynamic precipitation. Therefore, this region continues to maintain several β phases and hinders the migration of grain boundaries. The degree of dynamic precipitation in the region far from the

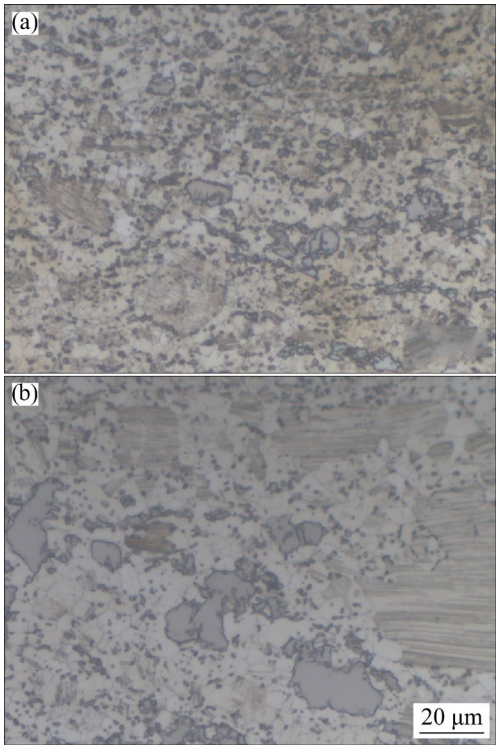

Fig. 10 OM metallographic images depicting gauge section of original specimen after tensile test at 400 °C: (a) Region near fracture surface; (b) Region far from fracture surface

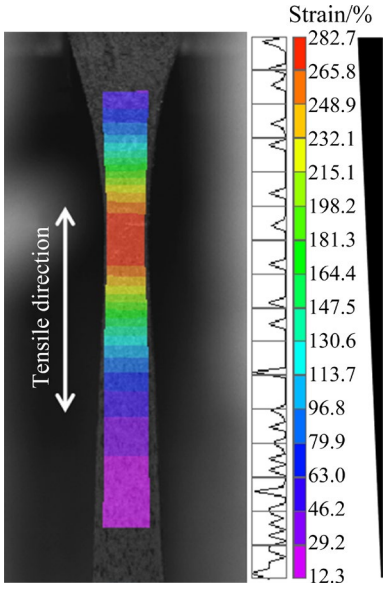

Fig. 11 Strain distribution of gauge section of specimen during high-temperature tensile process

fracture surface is low. Therefore, the number of β phases cannot be retained at high temperatures over a long duration. Moreover, the DRX degree near the fracture surface is high, and the new grains further refine the structure. Therefore, under comprehensive action, the average grain size in this region only slightly increases.

Figure 12 presents the OM metallographic images depicting the gauge sections of the 2-MDFed specimens after the tensile test at different temperatures. Overall, the LPSO phases in each region of the MDFed specimen after the tensile test are further refined to varying degrees, and the proportion of the matrix structure further increases. The average grain size (d) and proportion of β phase (P_β) are marked in the images. As the strain distribution characteristics are the same, the differences in the microstructures near and far from the fracture surface of the MDFed specimen after the tensile test are consistent with those of the original specimen. However, the initial grain size of the MDFed alloy is lower and the initial proportion of β phases is higher than those of the original alloy. Moreover, further DRX and dynamic precipitation occur during the tensile process. The MDF treatment yields several discrete elements in the MDFed alloy, and the LPSO phases are further refined during the tensile process. The composition basis of dynamic precipitation in the MDFed alloy is better than that of the original alloy. Thus, the grain size of the MDFed alloy remains small during the tensile process. After the tensile test at 375 °C,

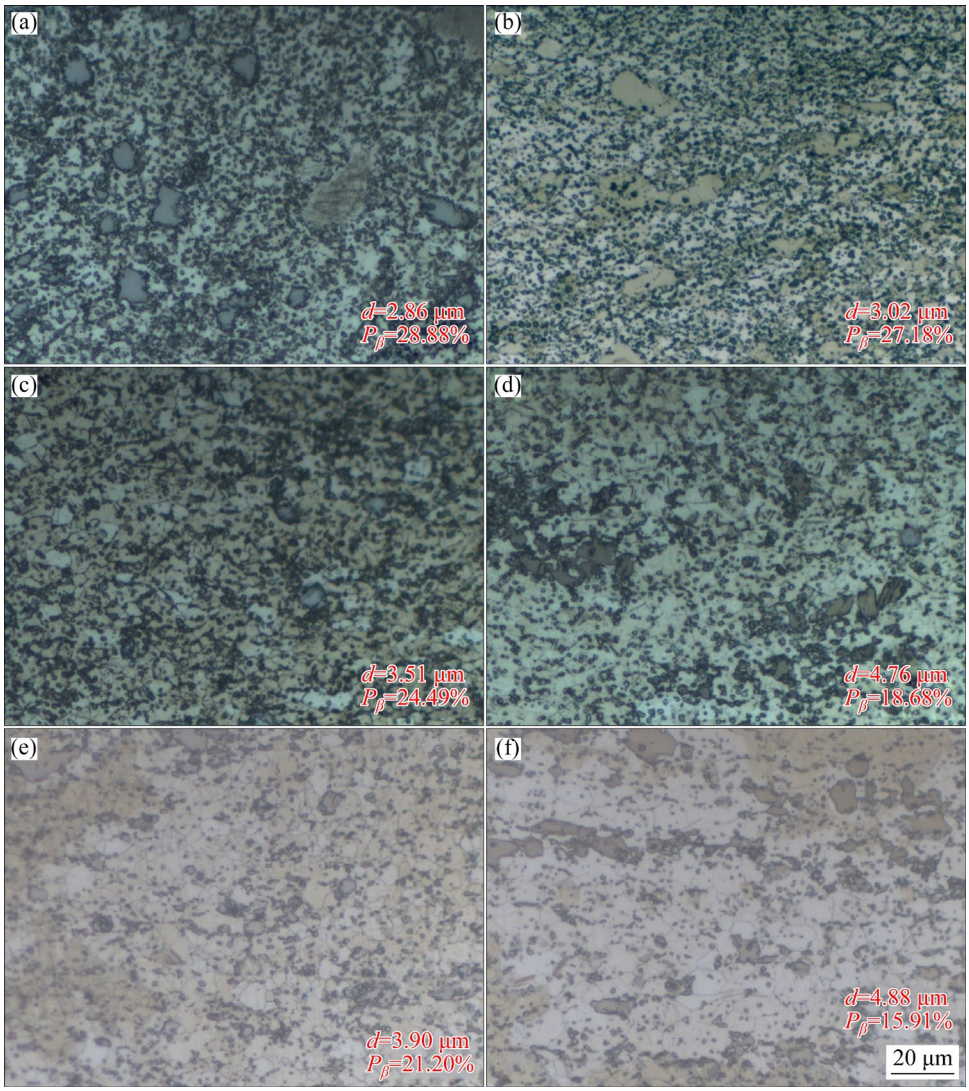

Fig. 12 OM metallographic images depicting gauge sections of 2-MDFed specimens after tensile test at different temperatures: (a) 300 °C, region near fracture surface; (b) 300 °C, region far from fracture surface; (c) 375 °C, region near fracture surface; (d) 375 °C, region far from fracture surface; (e) 400 °C, region near fracture surface; (f) 400 °C, region far from fracture surface

the grain size near the fracture surface is approximately 3.51 μm, which is slightly larger than 3.27 μm before the tensile test. After the tensile test at 400 °C, the grain size near the fracture surface reaches approximately 3.90 μm. The decrease in the specimen elongation at 400 °C can be attributed to the increase in the degree of grain growth.

The microstructure of the specimen after the tensile test at 300 °C is special, which is manifested in the relatively low refinement degree of the LPSO phases in each region and the low average grain size. The deformation temperature of this specimen is low, and the deformation duration is short. The DRX is insufficient. Therefore, the LPSO phases only exhibit low degrees of refinement. Temperature decreases cause serious dislocation pile-up and promote the precipitation of the β phases. The solid solubility of related elements at low temperatures is low. Therefore, the composition basis of dynamic precipitation is sufficient. Furthermore, the driving force of grain growth at low temperatures is low. Therefore, the grain size in each region of the specimen is small. However, this fine-grained structure does not increase the elongation of the specimen. According to the m value, GBS does not start at 300 °C. Therefore, the promotion effect of the high-density grain boundary in the fine-grained structure on GBS does not occur.

The above analysis elucidates the role of the β phases in the high-temperature tensile process of such an alloy. Next, TEM was employed for in-depth analysis of the β phases. Figure 13 presents the TEM image of the region near the fracture surface of the 2-MDFed specimen after the tensile test at 375 °C. Several fine, spherical second phases exhibit dispersive distribution in the region presented in Fig. 13(a). The selected area electron diffraction (SAED) pattern of the phase marked by the yellow arrow is shown in Fig. 13(b), indicating the presence of a β-Mg_5Gd-type second phase. The regulation mechanism of the β phase to grain size is further demonstrated in Fig. 13(a). First, as depicted by the white arrows in Region *A*, the β phases hinder the convex and concave migrations of the grain boundaries, thereby limiting grain growth. Second, in Regions *B* and *C*, the dislocations surrounded by multiple β phases are stacked and entangled into multiple small-sized subgrains, which is consistent with the continuous DRX mechanism [33]. More specifically, during the high-temperature tensile process, the β phases can effectively limit grain growth and directly participate in microstructural refinement by promoting DRX. These are the two main mechanisms by which the β phases regulate grain size.

Four grains are marked in Region *A* presented in Fig. 13(a), and some grain boundaries are marked with white dashed lines. The dislocation densities in Grains 1, 2, and 4 are relatively uniform, and the four subgrains with different dislocation densities are arranged along the grain boundary in Grain 3. According to the study conducted by ANDO et al [34], the generation of such subgrains is related to the rearrangement of basal and cylindrical dislocations originating from GBS activity, which proves the occurrence of GBS and indicates the activation of the multi-type dislocation movement.

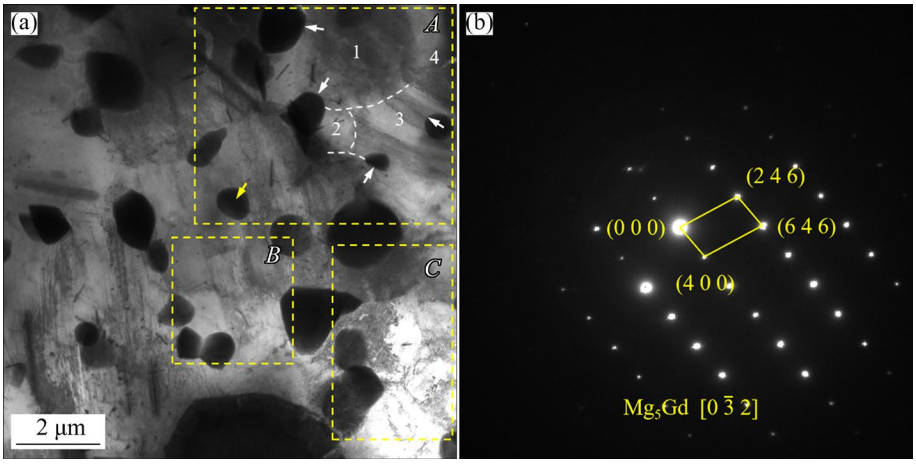

Fig. 13 TEM image of region near fracture surface of 2-MDFed specimen after tensile test at 375 °C: (a) BF-TEM image; (b) SAED pattern of marked phase

The indexes obtained in Section 3.2 indicate that the main mechanism of superplastic deformation in the MDFed alloys is GBS, accompanied by vacancy diffusion creep. The large proportion of the fine-grained matrix structure resulting from severe plastic deformation is beneficial for GBS, which is the main reason for the better superplasticity of the MDFed alloys than the original alloy. Based on the small initial grain size, the large initial proportion of the β phases, and further DRX and dynamic precipitation during the high-temperature tensile process, the microstructural stability of the MDFed alloy is better than that of the original alloy, thereby guaranteeing superplastic deformation. Notably, obvious microstructural flow lines are observed in the original alloy (see Fig. 8), which is a common feature of the microstructures obtained via most traditional deformation processes [35,36]. However, all types of phase structures within the microstructure of the MDFed alloy exhibit random distributions, without a strong basal texture, and a multi-texture component state is observed [23], which is conducive to uniform tensile deformation.

Figure 14 presents the SEM images depicting the gauge sections of the 2-MDFed specimens that have undergone the tensile test at different temperatures, revealing a different type of evolution. In the specimens after tensile tests at 375 and 400 °C, many white particles exhibit dispersive distribution in the region near the fracture surface (Figs. 14(c) and 14(e)). In contrast, few particles are distributed in the region far from this surface (Figs. 14(d) and 14(f)). Furthermore, only a few white particles are observed in the images of the specimen tested at 300 °C (Figs. 14(a) and 14(b)). The high-magnification image of the region marked by the yellow dotted box in Fig. 14(e) is presented in Fig. 14(g). Most of the white particle phases in the image appear cubic, and a few particles appear spherical. The energy-dispersive X-ray spectroscopy (EDS) data of the phases marked in Fig. 14(g) are listed in Table 1. The cubic white particle phases (I and V) are considered Y-rich phases owing to their

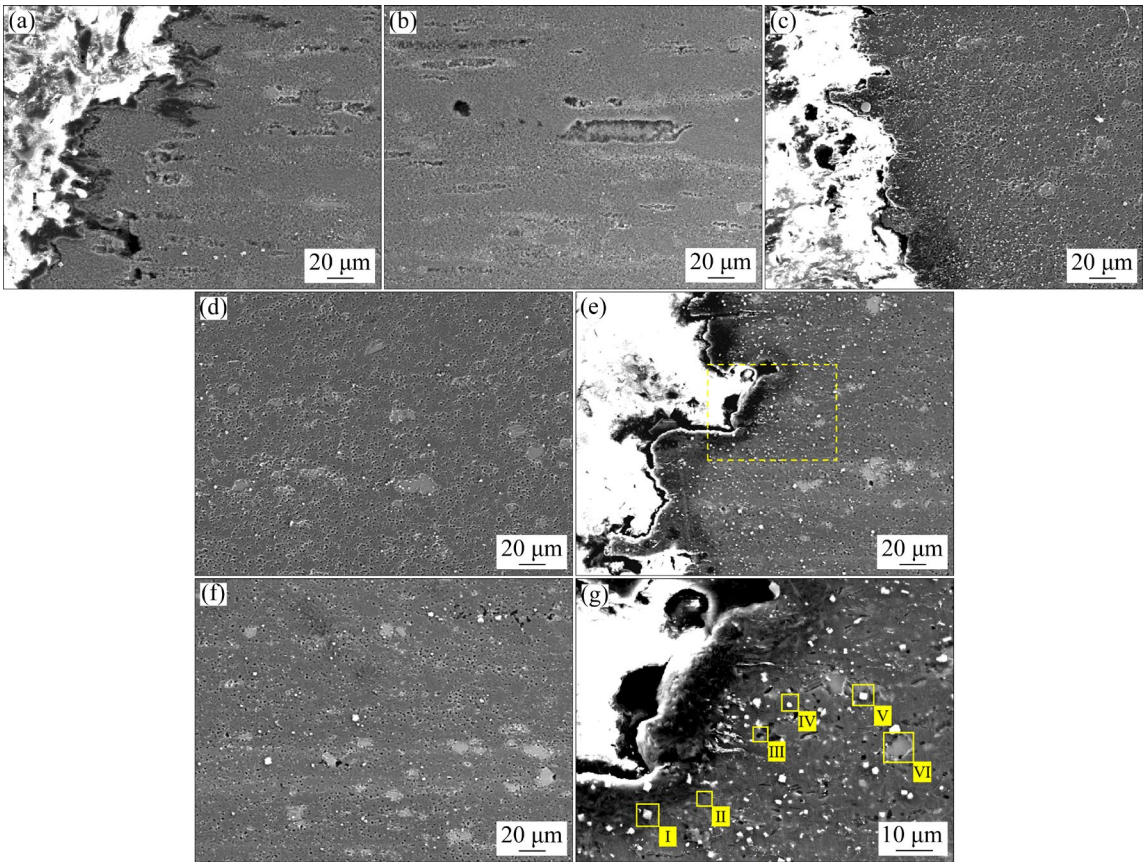

Fig. 14 SEM images depicting gauge sections of 2-MDFed specimens after tensile test at different temperatures: (a) 300 °C, region near fracture surface; (b) 300 °C, region far from fracture surface; (c) 375 °C, region near fracture surface; (d) 375 °C, region far from fracture surface; (e) 400 °C, region near fracture surface; (f) 400 °C, region far from fracture surface; (g) High-magnification image of region identified by yellow dotted box in (e)

high Y content. The composition of the spherical white particle phase (IV) is close to $Mg_5(Gd, Y)$, which could be attributed to the partial substitution of Y for Gd based on β-Mg_5Gd [37]. Moreover, no phase is present at Position II, and the EDS data indicate that the α-Mg matrix containing Gd and Y is present at this position. Position III represents a black circular structure located at the grain boundary, and the data are close to that of the matrix. This structure is possibly the erosion pit formed owing to the corrosion of the β phase [38], which does not affect the tensile process. The data of the block phase at Position VI are consistent with 18R-LPSO [39]. This type of phase is significantly refined during the tensile process and randomly distributed in a small-sized block shape.

Table 1 EDS results obtained from marked positions in Fig. 14(g) (at.%)

Position	Mg	Gd	Y	Zn	Zr	Determined phase
I	44.89	16.29	37.64	0.44	0.75	Y-rich
II	97.49	1.18	0.90	0.38	0.05	α-Mg
III	97.45	1.18	0.88	0.44	0.04	Erosion pit
IV	86.39	7.83	5.78	–	–	β
V	57.71	12.71	28.28	0.69	0.61	Y-rich
VI	88.60	4.02	3.95	3.38	0.05	Bulk LPSO

The Y-rich phase that is thermally stable, hard, and brittle, is often reported to be present in rare-earth magnesium alloys after hot deformation or heat treatment [40,41]. Based on the above analysis, the specimens tested at 375 and 400 °C still precipitated many Y-rich phases under the condition of high solid solubility of the elements. The differences between these two sets of tests and the tensile test at 300°C are high temperature and large strain (superplastic deformation). Therefore, these two conditions are important for the precipitation of large amounts of Y-rich phases. The region near the fracture surface is a high-strain zone during tension. Therefore, the amount of Y-rich phase precipitate in this region is higher than that in the region far from the fracture surface.

3.4 Fracture behavior and influencing mechanisms

Figure 14 demonstrates that several cavities extend along the tensile direction in the gauge section of the 2-MDFed specimen after the tensile test at 300 °C. However, the cavities are almost absent in the specimens after the tensile test at 375 and 400 °C. The SEM images shown in Fig. 15 depict the cavities in the gauge section of the 2-MDFed specimen after the tensile test at 300 °C. As indicated by the arrows in Fig. 15(a), LPSO phases are present at the ends of most cavities. During the tensile process at 300 °C, the deformation is regulated via dislocation creep, and the dislocation density in the structure is high. However, the refinement degrees of the LPSO phases are low, which hinders the movement of dislocations and generates stress concentrations, thereby inducing cavity nucleation. Furthermore, the elastic modulus of the LPSO phase is higher

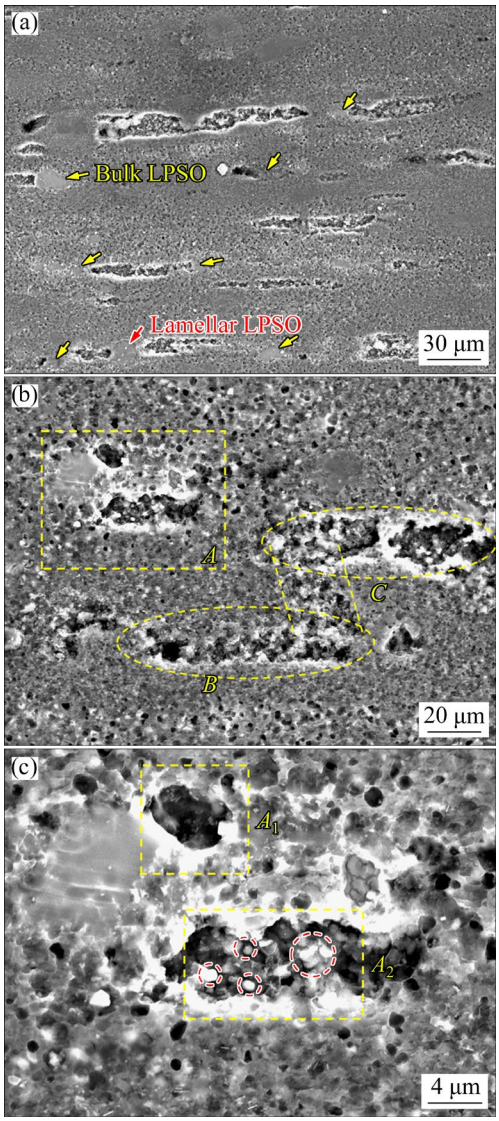

Fig. 15 SEM images depicting cavities in gauge section of 2-MDFed specimen after tensile test at 300 °C: (a, b) Images of two different regions; (c) High-magnification image of Region *A* in (b)

than that of the matrix [42], and the resulting uneven deformation easily promotes the formation of cavities. The high-magnification image of Region *A* in Fig. 15(b) is presented in Fig. 15(c). The cavity in Region A_1 nucleates at the phase boundary of the bulk LPSO. The nearly elliptical shape of this cavity indicates that it is in the transition stage from diffusion-controlled to plastic-controlled growth [43]. The large cavity in Region A_2 elongates along the tensile direction, and many clear β phases are present in this cavity, as indicated by the red dashed circles. The cavity expands under plastic deformation, including radial and mainly axial, and the tortuous boundary indicates that the expansion direction dynamically changes. At 300 °C, the β phases are stable [44] and densely distributed at the grain boundaries, and the phase boundaries are favorable positions for cavity nucleation. The phase boundaries of the β phases distributed on the expansion path of the large cavities could be easily separated from the matrix under the action of stress, thereby creating a favorable path for the expansion of the cavities. Thus, the cavities have formed a tortuous boundary. In Fig. 15(b), Cavity *B* extends along the tensile direction with the same tortuous boundary, whereas Cavity *C* is composed of two sub-cavities that are not yet fully connected. Local stress concentrations may generate secondary cracks in the overlapping area between Cavities *B* and *C*. These cracks can expand under plastic deformation, connecting the two cavities, which also reflects the final fracture mechanism of the specimen.

Figure 16 presents the SEM images depicting the fracture surfaces of the 2-MDFed specimens after the tensile test at different temperatures. As shown in Fig. 16(a), several dimples are present on the fracture surface of the specimen after the tensile test at 300 °C, which is the characteristic of ductile fracture, and a small area of the cleavage structure is present in Region *A* displayed in the lower part of the image. The high-magnification image of Region *I* in Fig. 16(a) is shown in Fig. 16(b). The red arrows mark the snake-like stripes on the inner surface of the dimples, which indicate that the dimple walls undergo further plastic deformation during expansion and extension [45]. The dimples are connected by ridge structures. The ridge structure in Region *B* exhibits a tear state reflecting good plasticity, whereas those in Regions *C* and *D* show a smooth shear state, with micro-cleavage surfaces surrounding these structures. When local dislocations that cannot effectively diffuse are present between dimples, the connection will be completed in the form of cleavage fracture and attain a smooth shear ridge [45,46].

The fracture morphology indicates that the 2-MDFed specimen undergoes ductile fracture at

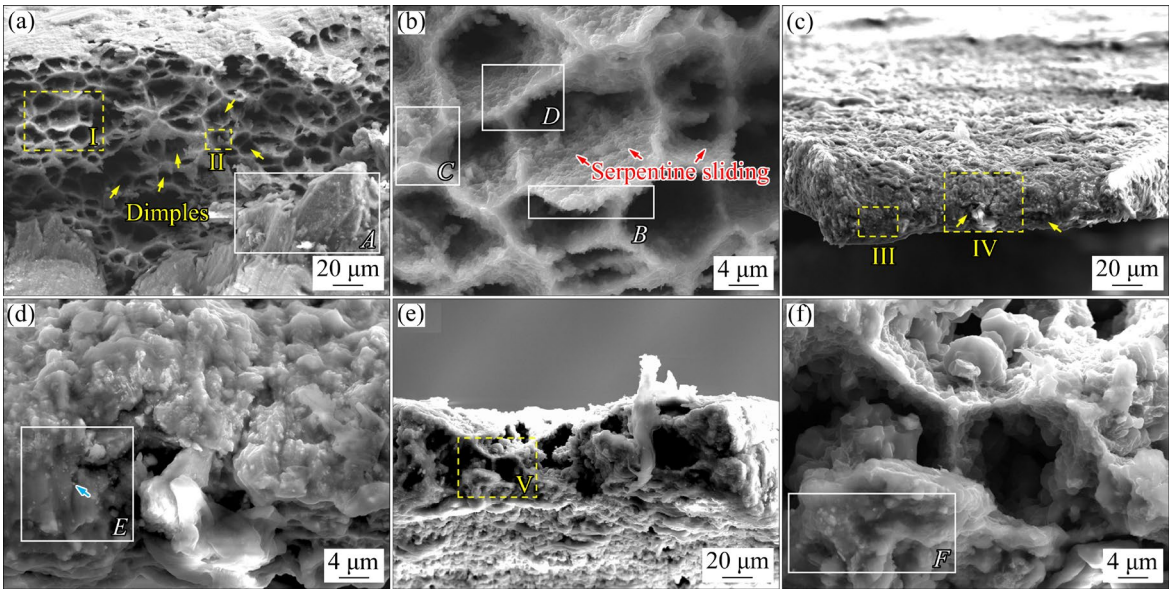

Fig. 16 SEM images depicting fracture surface of 2-MDFed specimens after tensile test at different temperatures: (a) Fracture surface of specimen after tensile test at 300 °C; (b) High-magnification image of Region I; (c) Fracture surface of specimen after tensile test at 375 °C; (d) High-magnification image of Region IV; (e) Fracture surface of specimen after tensile test at 400 °C; (f) High-magnification image of Region V

300 °C, which corresponds to a high elongation of approximately 129%. However, the local region of the fracture surface exhibits cleavage characteristics. The tensile fracture behavior of the 2-MDFed alloy at 300 °C can be briefly summarized as follows. At the initial deformation stage, several cavities nucleate at various interfaces. The progress of deformation and the favorable path provided by the β phases cause the cavities to continue expanding and connecting. As GBS is inactive, the cavities reach the deformation limit before achieving a high degree of aggregation and expansion, and partial cleavage fracture occurs due to local dislocation pile-up. The 2-MDFed alloy exhibits good plasticity and high elongation at 300 °C. However, the elongation does not reach the superplastic standard.

When the tensile temperature increases to 375 and 400 °C, the elongation of the specimen considerably improves. Figure 16(e) shows that the fracture surface of the specimen after the tensile test at 400 °C also exhibits noticeable ductile fracture characteristics. However, the depths and sizes of the dimples are substantially larger, corresponding to a high elongation of approximately 429%, than those of the specimen after tensile test at 300 °C. The high-magnification image of Region V is presented in Fig. 16(f). The dimples are connected by tearing ridges, and the equiaxed grains present in the dimples indicate that the initial cavities nucleate at the grain boundaries. Figure 16(c) shows that only a few deep cavities are present in the middle of the fracture surface of the specimen after the tensile test at 375 °C. The high-magnification image of Region IV is presented in Fig. 16(d). Except for the presence of a few cavities, most of the regions exhibit intergranular fracture structures with local microcracks.

GBS is fully activated at 375 and 400 °C, which is conducive to achieving high elongation. In the early stage of deformation, the vacancies associated with GBS can be fully transferred via grain boundary or lattice diffusion, which effectively delays the nucleation of intergranular cavities. The refinement degrees of the LPSO phases are relatively high at 375 and 400 °C, and the number of cavities induced is substantially reduced. However, the stability of the structure at 400 °C is slightly reduced, and the increase in the grain size increases the diffusion distance required for GBS regulation. Therefore, as deformation progresses, several microcavities begin to nucleate at the grain boundaries. These microcavities become highly aggregated and expand into large-sized deep cavities until the cavity walls (dimple walls) fail to withstand deformation and fracture. The stable fine-grained structure of the specimen at 375 °C effectively inhibits the generation of several cavities, and the gauge section diffusely elongates to a fine-tip shape, yielding excellent elongation with a maximum value of 693%. The final fracture can be attributed to a micropore aggregation fracture in the middle of the fracture surface and an intergranular fracture in the other regions.

Figure 17(a) presents the high-magnification image of Region II shown in Fig. 16(a). As indicated by the white arrows, several spherical β phases are present on the dimple wall, which is consistent with the results obtained from the previous analysis, revealing that stable β phases create favorable paths for the expansion of cavities (dimples). A pit is present at the junction of the ridge structure in the lower left region of Fig. 17(a), with the pit wall in a cleavage fracture state. A cubic

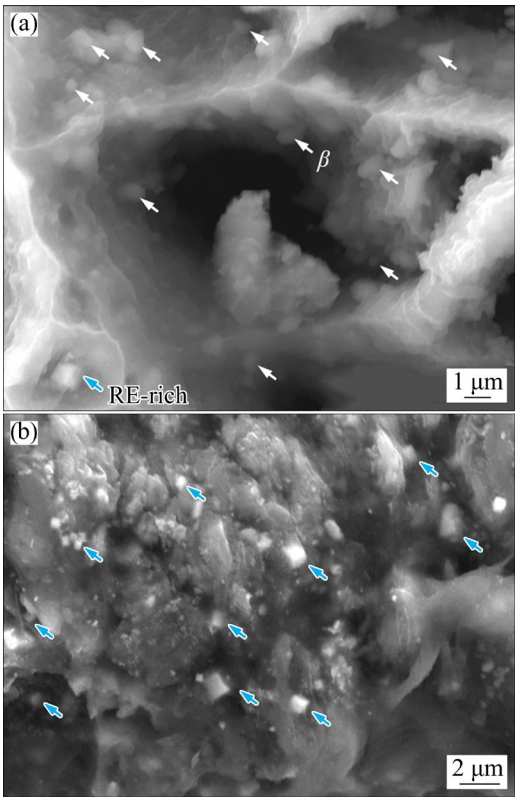

Fig. 17 High-magnification SEM images of some regions on fracture surface: (a) Region II in Fig. 16(a); (b) Region III in Fig. 16(c)

Y-rich phase is marked by a blue arrow at the bottom of the pit in the image. This phase may have accelerated the fracture of the dimple wall. For the specimens after the tensile tests at 375 and 400 °C, several Y-rich phases are precipitated near the fracture surfaces, and the fracture morphologies indicate that this evolution profoundly affected the tensile process. An intergranular crack is observed in Region *E* of Fig. 16(d), and the Y-rich phase marked by the blue arrow appears to act as the nucleation point of the crack. The high-magnification image of Region III (intergranular fracture zone) in Fig. 16(c) is displayed in Fig. 17(b), and the blue arrows indicate several Y-rich phases located at the bottom parts of the pits, distributed on the crack path or protruding in the matrix, i.e., the Y-rich phases may have accelerated the intergranular fracture at 375 °C. In addition, several Y-rich phases are present on the tearing ridge in Region *F*, as shown in Fig. 16(f), suggesting that this type of phase also considerably impacts the fracture at 400 °C.

The Y-rich phase in the 2-MDFed specimen after tensile test at 375 °C is characterized through TEM, as shown in Fig. 18. Figure 18(a) shows the high-angle annular dark-field scanning transmission electron microscopy (HAADF-STEM) image of the Y-rich phase, and the element distribution map indicates substantial Y enrichment within this phase. The dark-field high-resolution TEM (DF-HRTEM) image of Region *A* (phase boundary) is presented in Fig. 18(b), and the Y-rich phase contains a face-centered cubic structure, as determined using fast Fourier transform (FFT). A relative orientation relationship exists between the $(020)_{\text{Y-rich}}$ crystal plane and the adjacent $(10\bar{1}0)_{\alpha\text{-Mg}}$ crystal plane along the $(\bar{2}00)_{\text{Y-rich}}$ crystal plane, with an angle of approximately 30°. The degree of lattice mismatch (δ) can be calculated using Eq. (4) [47,48]:

$$\delta=(d_2/\sin\theta-d_1)/d_1 \quad (4)$$

where d_2 and d_1 denote interplanar spacings of $(10\bar{1}0)_{\alpha\text{-Mg}}$ and $(020)_{\text{Y-rich}}$, respectively, and θ denotes the angle between $(10\bar{1}0)_{\alpha\text{-Mg}}$ and $(\bar{2}00)_{\alpha\text{-Mg}}$. The calculated δ is approximately 25.9%, which indicates an incoherent relationship. Based on this relationship, the bonding degrees of the atoms on both sides of the interface are low, and the interface energy is high.

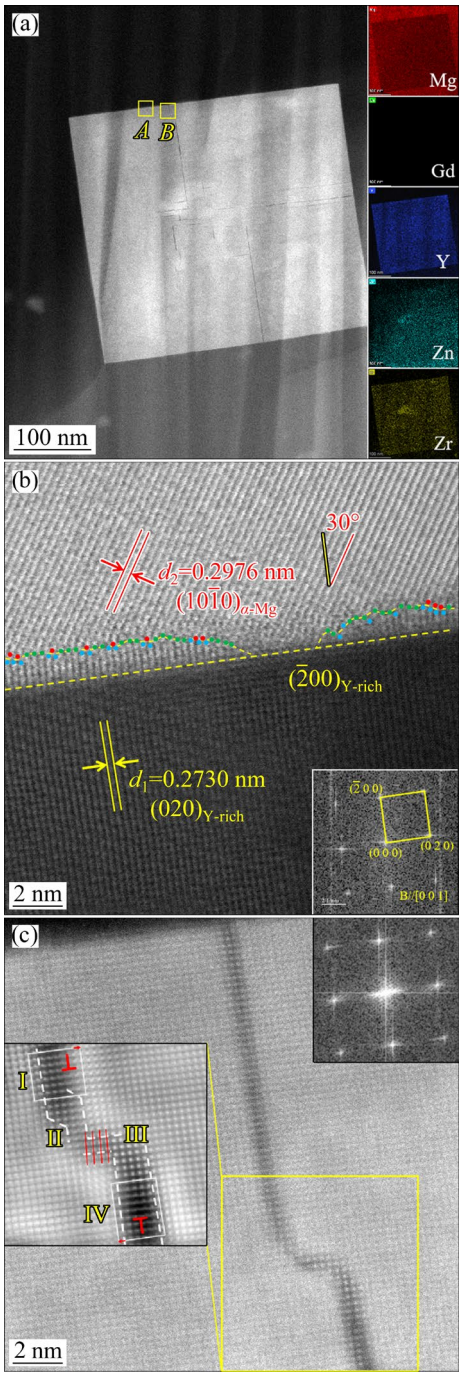

Fig. 18 TEM images of Y-rich phase in 2-MDFed specimen after tensile test at 375 °C: (a) HAADF-STEM image (Embedded images are distribution maps of main elements); (b) DF-HRTEM image of Region *A* (embedded image is FFT pattern of Y-rich phase); (c) HAADF-HRTEM image of Region *B* (Embedded image in upper right corner is FFT pattern, and that in left corner is IFFT image of selected region)

Further observation reveals that protrusions are present at the local boundary of the Y-rich phase. These protrusions are formed by the unequal extensions of some $(020)_{\text{Y-rich}}$ crystal planes by

1−2 nm and the matching relationship between the corresponding $(020)_{\text{Y-rich}}$ and $(10\bar{1}0)_{\alpha\text{-Mg}}$ crystal planes changes. The endpoints of the crystal planes that maintain matching (possibly distortion-type matching) are roughly marked with green dots in Fig. 18(b), and the endpoints of the unmatched $(020)_{\text{Y-rich}}$ and $(10\bar{1}0)_{\alpha\text{-Mg}}$ crystal planes, with mismatched dislocations, are marked with blue and red dots, respectively. The protrusions on the boundary are essentially generated based on the principle of energy minimization, forming more matches through the unequal extension of crystal planes to reduce interface energy, whereas the formation of mismatched dislocations can theoretically consume dislocations accumulating at the phase boundary. However, the protrusions increase the area of the phase boundary, thereby weakening the energy reduction effect. Therefore, these protrusions are only formed at the partial boundaries. Figure 18(a) shows several dark lines in the Y-rich phase, and the high-magnification HAADF-HRTEM image of Region *B* is displayed in Fig. 18(c). The diffraction lines in the FFT pattern indicate that the dark lines are stacking faults. The embedded image on the left side in Fig. 18(c) shows the inverse FFT (IFFT) image of the selected region. The right side of stacking fault I is a frank dislocation with magnitude of Burgers vector b=1/3[020]. The formation of this dislocation may lead to step climbing from stacking faults I to II, and the magnitude of Burgers vector of the frank dislocation in stacking fault IV is $b=1/3[0\bar{2}0]$. The distortion of the atomic arrangement in the overlapping region between stacking faults II and IV is large, which yields stacking fault III. The stacking faults within the Y-rich phase may be related to the dislocation pile-up near the phase boundary [49,50]. When the dislocation pile-up reaches a certain critical degree, the generation of stacking faults will be promoted. In addition, Y enrichment leads to the low stacking fault energy of the Y-rich phase. A relevant study [49] reported that too many stacking faults in a phase generate shear force dipoles and accelerate the shear breakage of the phase.

At high temperatures, GBS is fully activated, the dislocation density is low, and the diffusion ability increases. Therefore, the dislocation pile-up phenomenon at 375 and 400 °C is weaker than that at 300 °C. However, the precipitation of several Y-rich phases considerably hinders the movement of dislocations, and two types of evolutions possibly occur. First, the separation trend between the phase boundary and the matrix with high energy and a low bonding-degree matching relationship increases; the regulating effect of the protrusion is limited. Second, many stacking faults are generated inside the Y-rich phase, resulting in the break of the Y-rich phase. These evolutions result in the formation of micro-cracks and micro-voids between grains, which accelerates the fracture of the specimen.

As can be seen from Figs. 16 and 17, only a few β phases exist on the fracture surfaces of the specimens after the tensile test at 375 and 400 °C, i.e., the β phases may only have a limited effect on the fracture behavior of the specimen at high temperatures. According to the analysis, the β phase is in a stable state at 300 °C, and high-density dislocations accumulate at its boundary, promoting the nucleation and expansion of cavities. As the temperature increases, the stability of the β phase decreases, and theoretically, its deformation compatibility with the matrix improves.

Figure 19 displays the HRTEM images of β phase and its adjacent matrix present in the 2-MDFed specimen after the tensile test at 375 °C. Figure 19(a) shows the local region of β phase, and the image can be divided into four parts, i.e., *A*, *B*, and *C* are the central part, outer part, and matrix adjacent to the β phase, respectively, and *D* is the slip zone between the β phase and the matrix. According to the geometric phase analysis (GPA) image shown in Fig. 19(b), the central and outer parts of the β phase have no strain and a large strain, respectively. Figure 19(c) demonstrates that the lattice distortion of the central and outer parts of the β phase is low and high, respectively, and several dislocations are present in the outer part, which is consistent with the strain distribution characteristics presented in Fig. 19(b). The spots in Fig. 19(d) are annularly distributed, i.e., polycrystalline features are present, and the corresponding crystal planes are marked. In addition, a halo is present. The corresponding Fig. 19(g) shows that several nanocrystals are present, and the inter-nanocrystal structure exhibits a disordered near-amorphous state. As can be seen from Figs. 19(e) and 19(h), a few nanocrystals are present in the slip zone, and the degree of disorder in this zone is higher than that in

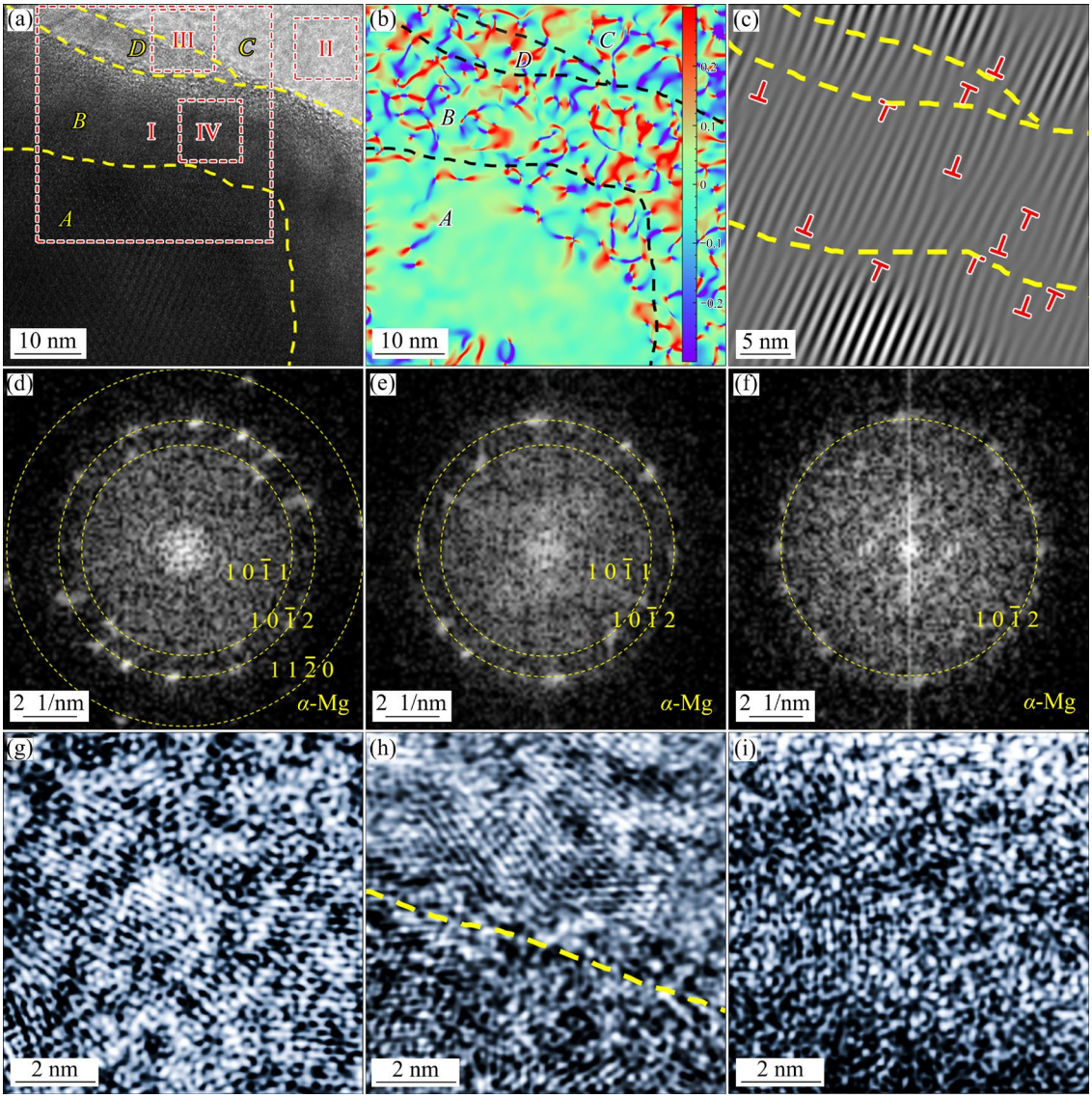

Fig. 19 HRTEM images of β phase and its adjacent matrix present in 2-MDFed specimen after tensile test at 375 °C: (a) DF-HRTEM image; (b) GPA image; (c) Spot mask-lattice fringe image of Region I; (d−f) FFT patterns of Regions II, III and IV, respectively; (g−i) Bandpass mask-IFFT images of Regions II, III and IV, respectively

the matrix. Figure 19(f) shows an obvious halo and considerably weakened polycrystalline spots, and no obvious arrangement structure is observed in Fig. 19(i). According to the analysis, high temperature and large strain promote the nucleation of nanocrystals in the adjacent matrix, which is beneficial for GBS. As the deformation proceeds, many disordered atoms diffuse into the slip zone, and this high degree of the near-amorphous structure plays an excellent lubricating role during the relative sliding between the β phase and the matrix, thereby promoting superplasticity. High temperature causes the outer layer of the β phase to soften and undergo large deformation due to stress during the tensile process. The original structure of the complete atomic arrangement is destroyed, the stress concentration is alleviated, and the deformation is effectively coordinated.

4 Conclusions

(1) After MDF at a temperature of 350 °C and strain rates of 0.1 and 0.01 s^{-1}, the superplasticity of the alloy can be significantly improved. The elongations of the MDFed alloys exceed 400% under tensile conditions with a strain rate of 6.06×10^{-4} s^{-1} and temperatures of 350, 375 and 400 °C, and reach the maximum values of 766%

(1-MDFed) and 693% (2-MDFed) at 375 °C.

(2) The m values of the alloys increase from 0.4−0.5 before MDF to 0.5−0.7 after MDF, and the GBS of the MDFed alloy is sufficient. The Q values decrease from 180−300 kJ/mol to 110−160 kJ/mol, suggesting that the energy barrier of deformation decreases. At 350 and 375 °C, the main regulatory mechanisms of GBS in the MDFed alloys are lattice and grain boundary diffusions, respectively. At 400 °C, both diffusion mechanisms play regulatory roles.

(3) The MDFed alloy undergoes ductile fracture with several dimples at 300 °C. As GBS is inactive, several cavities nucleate and fail to sufficiently aggregate and expand; the alloy exhibits high elongation but does not reach the superplasticity standard. As the temperature increases, GBS is activated. At 375 °C, the stable fine-grained structure effectively coordinates GBS and diffuses vacancies, thereby inhibiting the generation of several cavities, and the fracture mode is a combination of microporous aggregation and intergranular fracture. The grains grow at 400 °C and therefore, the cavities extensively nucleate and are highly aggregated. The alloy undergoes ductile fracture, and the depth and size of the dimples are deeper and larger than those at 300 °C.

(4) The β phase maintains the stability of the fine-grained structure by limiting grain growth and promoting DRX. The number of β phases decreases with the increase in temperature; thus, the grain size increases. The β phase is stable at 300 °C, and the cavities easily nucleate at its boundary. However, the β phase softens at high temperatures, which alleviates the stress concentration. The Y-rich phase extensively nucleates in the high-strain region (i.e., the final fracture region) at high temperatures, and the resulting dislocation accumulation causes this phase to break and separate from the matrix, accelerating the fracture of the specimen.

CRediT authorship contribution statement

Jing-qi ZHAO: Investigation, Data curation, Writing − Original draft preparation, Writing − Review & editing; **Ze-zheng WANG:** Investigation, Data curation; **Chun KE:** Formal analysis; **Qiang MENG:** Validation, Visualization; **Chun-xiang ZHANG:** Resources; **Jun-ting LUO:** Conceptualization, Supervision, Project administration, Writing − Review & editing.

Declaration of competing interest

The authors declare that they have no known competing financial interests or personal relationships that could have appeared to influence the work reported in this paper.

Acknowledgments

This work was supported by the National Natural Science Foundation of China (No. 52127808).

References

[1] YANG Yan, XIONG Xiao-ming, CHEN Jing, PENG Xiao-dong, CHEN Dao-lun, PAN Fu-sheng. Research advances in magnesium and magnesium alloys worldwide in 2020 [J]. Journal of Magnesium and Alloys, 2021, 9(3): 705−747.

[2] SONG Jiang-feng, CHEN Jing, XIONG Xiao-ming, PENG Xiao-dong, CHEN Dao-lun, PAN Fu-sheng. Research advances of magnesium and magnesium alloys worldwide in 2021 [J]. Journal of Magnesium and Alloys, 2022, 10(4): 863−898.

[3] MALIK A, WANG Yang-wei, CHENG Huan-wu, NAZEER F, KHAN M A. What is the major problem with wrought Mg alloys? [J]. Results in Engineering, 2020, 7: 100162.

[4] GHAZISAEIDI M, HECTOR JR L G, CURTIN W A. Solute strengthening of twinning dislocations in Mg alloys [J]. Acta Materialia, 2014, 80: 278−287.

[5] NAZEER F, LONG Jian-yu, YANG Zhe, LI Chuan. Superplastic deformation behavior of Mg alloys: A review [J]. Journal of Magnesium and Alloys, 2022, 10(1): 97−109.

[6] XING H L, WANG C W, ZHANG K F, WANG Z R. Recent development in the mechanics of superplasticity and its applications [J]. Journal of Materials Processing Technology, 2004, 151(1/2/3): 196−202.

[7] JEONG H T, KIM W J. Critical review of superplastic magnesium alloys with emphasis on tensile elongation behavior and deformation mechanisms [J]. Journal of Magnesium and Alloys, 2022, 10(5): 1133−1153.

[8] VYSOTSKIY I, KIM K, MALOPHEYEV S, MIRONOV S, KAIBYSHEV R. Superplastic behavior of friction-stir welded Al−Mg−Sc−Zr alloy in ultrafine-grained condition [J]. Transactions of Nonferrous Metals Society of China, 2022, 32(4): 1083−1095.

[9] TAYLOR S, WEST G D, MOGIRE E, TANG F, KOTADIA H R. Superplastic forming characteristics of AZ41 magnesium alloy [J]. Transactions of Nonferrous Metals Society of China, 2021, 31(3): 648−654.

[10] SABBAGHIAN M, MAHMUDI R. Superplasticity of the fine-grained friction stir processed Mg−3Gd−1Zn sheets [J]. Materials Characterization, 2021, 172: 110902.

[11] ALIZADEH R, MAHMUDI R, PEREIRA P H R, HUANG Y, LANGDON T G. Microstructural evolution and superplasticity in an Mg−Gd−Y−Zr alloy after processing by different SPD techniques [J]. Materials Science and Engineering: A, 2017, 682: 577−585.

[12] LEE Shyong, CHIANG Chih-te, CHU Chun-lin, HSU Chang-chuan. Inter-granular liquid phase aiding grain

boundary sliding in superplastic deformation of fine-grained ZK60 Mg alloy [J]. Transactions of Nonferrous Metals Society of China, 2010, 20: s576−s579.

[13] YANG Jun-zhou, WU Jian-jun, XIE Hai-nan, LI Zhi-guo, WANG Kai-wei. Mechanism of continuous dynamic recrystallization of Ti−6Al−4V alloy during superplastic forming with sub-grain rotation [J]. Transactions of Nonferrous Metals Society of China, 2023, 33(3): 777−788.

[14] LUO Xuan, FENG Zong-qiang, YU Tian-bo, LUO Jun-qian, HUANG Tian-lin, WU Gui-lin, HANSEN N, HUANG Xiao-xu. Transitions in mechanical behavior and in deformation mechanisms enhance the strength and ductility of Mg−3Gd [J]. Acta Materialia, 2020, 183: 398−407.

[15] PENG Peng, WANG Bo, ZHOU Shi-bo, SHE Jia, TANG Ai-tao, ZHANG Jian-yue, PAN Fu-sheng. Effects of optimizing continuous forging extrusion process on the microstructure and mechanical properties of AZ31 magnesium alloy [J]. Materials Science and Engineering: A, 2022, 840: 142892.

[16] ZHANG Yu, HUANG Xiao-feng, LI Ya, MA Zhen-duo, MA Ying, HAO Yuan. Effects of samarium addition on as-cast microstructure, grain refinement and mechanical properties of Mg−6Zn−0.4Zr magnesium alloy [J]. Journal of Rare Earths, 2017, 35(5): 494−502.

[17] SUN Ming, HU Xiao-yu, PENG Li-ming, FU Peng-huai, PENG Ying-hong. Effects of Sm on the grain refinement, microstructures and mechanical properties of AZ31 magnesium alloy [J]. Materials Science and Engineering: A, 2015, 620: 89−96.

[18] CAO Fu-rong, XUE Guo-qiang, XU Guang-ming. Superplasticity of a dual-phase-dominated Mg−Li−Al−Zn−Sr alloy processed by multidirectional forging and rolling [J]. Materials Science and Engineering: A, 2017, 704: 360−374.

[19] MEHRABI A, MAHMUDI R, MIURA H. Superplasticity in a multi-directionally forged Mg−Li−Zn alloy [J]. Materials Science and Engineering: A, 2019, 765: 138274.

[20] LEE T J, KIM W J. Successful transition from low-temperature superplasticity to high-strain-rate superplasticity with increasing temperature in an ultrafine-grained Mg−Y−Zn−Zr alloy [J]. Journal of Alloys and Compounds, 2020, 817: 153298.

[21] YANG Q, XIAO B L, MA Z Y. Enhanced superplasticity in friction stir processed Mg−Gd−Y−Zr alloy [J]. Journal of Alloys and Compounds, 2013, 551: 61−66.

[22] LENG Zhe, ZHANG Jing-huai, LIN Hua-yi, FEI Peng fei, ZHANG Li, LIU Shu-juan, ZHANG Mi-lin, WU Rui-zhi. Superplastic behavior of extruded Mg−9RY−4Zn alloy containing long period stacking ordered phase [J]. Materials Science and Engineering: A, 2013, 576: 202−206.

[23] ZHAO Jing-qi, GUO Hao-shan, LUO Teng-teng, ZHANG Chun-xiang, LUO Jun-ting. Microstructure evolution and grain refinement mechanism of fine-grained Mg−Gd−Y−Zn−Zr alloy during multi-directional forging [J]. Journal of Alloys and Compounds, 2022, 928: 167199.

[24] SONG Jiang-feng, SHE Jia, CHEN Dao-lun, PAN Fu-sheng. Latest research advances on magnesium and magnesium alloys worldwide [J]. Journal of Magnesium and Alloys, 2020, 8(1): 1−41.

[25] JIA Jing-jing, ZHANG Hong-lei, MENG Mu, YANG Xue, ZHANG Xu-hui, ZHANG Zhi-min. Strain-induced heterogeneous bimodal microstructure behavior of Mg−Gd−Y−Zn−Zr alloy containing LPSO phase during hot compression [J]. Journal of Materials Research and Technology, 2023, 27: 4264−4277.

[26] WANG Xu, LI Ming, HUANG Yuan-chun, LIU Yu, HUANG Chang-qing. Deformation behavior of LPSO phases with regulated morphology and distribution and their role on dynamic recrystallization in hot-rolled Mg−Gd−Y−Zn−Zr alloy [J]. Journal of Materials Research and Technology, 2023, 26: 6121−6134.

[27] CHANG Zhi-yu, DENG Qing-chen, LAN Qiao, FENG Jian, LI Da-quan, LIU Bao-liang, WU Yu-juan, PENG Li-ming, DING Wen-jiang. Microstructure and mechanical properties of Mg−Gd−Y−Zn−Zr alloy prepared by rheo-diecasting [J]. Materials Science and Engineering: A, 2022, 848: 143287.

[28] YANG Q, XIAO B L, ZHANG Q, ZHENG M Y, MA Z Y. Exceptional high-strain-rate superplasticity in Mg−Gd−Y−Zn−Zr alloy with long-period stacking ordered phase [J]. Scripta Materialia, 2013, 69(11/12): 801−804.

[29] YANG H P, FU M W, TO S, WANG G C. Investigation on the maximum strain rate sensitivity (m) superplastic deformation of Mg−Li based alloy [J]. Materials & Design, 2016, 112: 151−159.

[30] BACKOFEN W A, TURNER I R, AVERY D H. Superplasticity in an Al−Zn Alloy [J]. Trans Asm, 1964, 57: 980−990.

[31] CHENG Liang, LI Jin-shan, XUE Xiang-yi, TANG Bin, KOU Hong-chao, BOUZY E. General features of high temperature deformation kinetics for γ-TiAl-based alloys with DP/NG microstructures: Part I. A survey of mechanical data and development of unified rate-equations [J]. Materials Science and Engineering: A, 2016, 678: 389−401.

[32] RAMEZANI S M, ZAREI-HANZAKI A, SALANDARI-RABORI A, ABEDI H R, MINARIK P, MÁTHIS K, HORVÁTH FEKETE K H. Unraveling the effect of deformation-induced phase transformation on microstructure and micro-texture evolution of a multi-axially forged Mg−Gd−Y−Zn−Zr alloy containing the LPSO phase [J]. Journal of Materials Research and Technology, 2021, 15: 2088−2101.

[33] XING Jie, SODA H, YANG Xu-yue, MIURA H, SAKAI T K. Ultra-fine grain development in an AZ31 magnesium alloy during multi-directional forging under decreasing temperature conditions [J]. Materials Transactions, 2005, 46(7): 1646−1650.

[34] ANDO D, SUTOU Y, KOIKE J. Internal microstructure observation of enhanced grain-boundary sliding at room temperature in AZ31 magnesium alloy [J]. Materials Science and Engineering: A, 2016, 666: 94−99.

[35] WANG Tao, YANG Lun, TANG Zhao-feng, WU Lei, YAN Huan-yuan, LIU Chao, MA Yun-zhu , LIU Wen-sheng, YU Zhao-ji. Microstructure, mechanical properties and deformation mechanism of powder metallurgy AZ31 magnesium alloy during rolling [J]. Materials Science and Engineering: A, 2022, 844: 143042.

[36] LI Yuan-qi, LI Feng, KANG Fu-wei, DU Hua-qiu, CHEN Zi-yu. Recent research and advances in extrusion forming of

magnesium alloys: A review [J]. Journal of Alloys and Compounds, 2023, 953: 170080.
[37] LI J P, YANG Z, LIU T, GUO Y C, XIA F, YANG J M, LIANG M X. Microstructures of extruded Mg−12Gd−1Zn−0.5Zr and Mg−12Gd−4Y−1Zn−0.5Zr alloys [J]. Scripta Materialia, 2007, 56(2): 137−140.
[38] CAO Geng-hua, ZHANG Da-tong, CHAI Fang, ZHANG Wei-wen, QIU Cheng. Superplastic behavior and microstructure evolution of a fine-grained Mg−Y−Nd alloy processed by submerged friction stir processing [J]. Materials Science and Engineering: A, 2015, 642: 157−166.
[39] ZHU Y M, MORTON A J, NIE J F. The 18R and 14H long-period stacking ordered structures in Mg−Y−Zn alloys [J]. Acta Materialia, 2010, 58(8): 2936−2947.
[40] ZHANG Li, ZHANG Jing-huai, XU Chi, LIU Shu-juan, JIAO Yu-feng, XU Long-jiang, WANG Yan-bo, MENG Jian, WU Rui-zhi, ZHANG Mi-lin. Investigation of high-strength and superplastic Mg−Y−Gd−Zn alloy [J]. Materials & Design, 2014, 61: 168−176.
[41] SHAHSA H, ZAREI-HANZAKI A, BARABI A, CHO J H, HAN S H. Dynamic dissolution and transformation of LPSO phase during thermomechanical processing of a GWZ magnesium alloy [J]. Materials Science and Engineering: A, 2019, 754: 85−98.
[42] TANE M, NAGAI Y, KIMIZUKA H, HAGIHARA K, KAWAMURA Y. Elastic properties of an Mg−Zn−Y alloy single crystal with a long-period stacking-ordered structure [J]. Acta Materialia, 2013, 61(17): 6338−6351.
[43] CHOKSHI A H. Cavity nucleation and growth in superplasticity [J]. Materials Science and Engineering: A, 2005, 410: 95−99.
[44] GRÖBNER J, KOZLOV A, FANG Xi-ya, ZHU Su-ming, NIE Jian-feng, GIBSON M A, SCHMID-FETZER R. Phase equilibria and transformations in ternary Mg−Gd−Zn alloys [J]. Acta Materialia, 2015, 90: 400−416.
[45] DENG Jiao, LIN Yong-cheng, LI Shui-sheng, CHEN Jian, DING Yi. Hot tensile deformation and fracture behaviors of AZ31 magnesium alloy [J]. Materials & Design, 2013, 49: 209−219.
[46] WEI Y H, WANG Q D, ZHU Y P, ZHOU H T, DING W J, CHINO Y, MABUCHI M. Superplasticity and grain boundary sliding in rolled AZ91 magnesium alloy at high strain rates [J]. Materials Science and Engineering: A, 2003, 360(1/2): 107−115.
[47] XU L D, DING S J, CAI X C, WU Y, LI Z J, WEN K K, XIN S W, SUN B R, HUANG M X, SHEN T D. Unveiling initial oxidation behavior of Mg−Y−Zn long-period stacking ordered (LPSO) phase [J]. Corrosion Science, 2022, 208: 110624.
[48] KIM T H, LEE S R, NAMKUMG S, JANG T S. A study on the Nd-rich phase evolution in the Nd−Fe−B sintered magnet and its mechanism during post-sintering annealing [J]. Journal of Alloys and Compounds, 2012, 537: 261−268.
[49] HAN Fu-zhou, LI Ge-ping, YUAN Fu-sen, GUO Wen-bin, REN Jie, WANG Qi-chen, ZHANG Ying-dong, MUHAMMAD A, LIU Cheng-ze, GU Heng-fei. Nano-refinement of the face-centered cubic $Zr(Fe,Cr)_2$ secondary phase particles in Zircaloy-4 alloy via localized-shearing/bending-driven fracture under high-temperature compression [J]. Journal of Materials Science & Technology, 2023, 165: 8−16.
[50] PENG J, WANG R C, ZHU M X, LI Z M, LIU H S, MUKHERJEE A K, HU T. 2430% Superplastic strain in a eutectic Au−Sn alloy with micrometer-sized grains maintained by spinodal-like decomposition [J]. Acta Materialia, 2022, 228: 117766.

多向锻造细晶 Mg−Gd−Y−Zn−Zr 合金的超塑性

赵静启[1]，王泽正[1]，柯 春[1]，孟 强[1]，张春祥[2]，骆俊廷[1,2]

1. 燕山大学 机械工程学院 先进锻压成形技术与科学教育部重点实验室，秦皇岛 066004；
2. 燕山大学 亚稳材料制备技术与科学国家重点实验室，秦皇岛 066004

摘 要：研究多向锻造前后 Mg−8.59Gd−3.85Y−1.14Zn−0.49Zr 合金的超塑性能，对影响超塑性变形的机制进行分析。结果表明：经过变形温度为 350 ℃、应变速率为 0.1 s^{-1} 和 0.01 s^{-1} (1-MDFed 和 2-MDFed)的多向锻造后，合金的超塑性可得到显著提升。多向锻造后合金在应变速率为 6.06×10^{-4} s^{-1}，温度为 350、375 和 400 ℃下的伸长率超过 400%，并在 375 ℃时达到 766%(1-MDFed)和 693%(2-MDFed)的最大伸长率。锻后合金的晶界滑移更充分，变形的能量势垒降低。β 相限制了晶粒生长并促进动态再结晶，保障细晶组织在超塑性变形过程中的稳定性。富 Y 相在高温下于高应变区(即最终断裂区)大量形核，加速了试样的断裂。

关键词：Mg−Gd−Y−Zn−Zr；超塑性；多向锻造；断口形貌；富 Y 相

(Edited by Xiang-qun LI)